Title

Dietary Iron Intake Has Long-Term Effects on the Fecal Metabolome and Microbiome

Authors

Kostenko, Anastasiia

Zuffa, Simone

Zhi, Hui

et al.

Publication Date

2024-07-11

DOI

10.1093/mtomcs/mfae033

Target: iScience
https://www.cell.com/iscience/home

Title: Dietary Iron Intake Has Long-Term Effects on the Fecal Metabolome and Microbiome

Authors: Anastasiia Kostenko[1], Simone Zuffa[2,3], Hui Zhi[4], Kevin Mildau[5,6], Manuela Raffatellu[2,4,7], Pieter C. Dorrestein[2,3], Allegra T. Aron[1,2,3]

Affiliations:
[1] Department of Chemistry and Biochemistry, University of Denver, Denver, CO, USA
[2] Skaggs School of Pharmacy and Pharmaceutical Sciences, University of California San Diego, La Jolla, San Diego, CA, USA
[3] Collaborative Mass Spectrometry Innovation Center, Skaggs School of Pharmacy and Pharmaceutical Sciences, University of California San Diego, La Jolla, CA, USA
[4] Department of Pediatrics, University of California San Diego, La Jolla, CA, USA
[5] Department of Analytical Chemistry, University of Vienna, Vienna
[6] Bioinformatics Group, Wageningen University & Research, 6708 PB, Wageningen, the Netherlands
[7] Chiba University-UC San Diego Center for Mucosal Immunology, Allergy, and Vaccines (CU-UCSD cMAV), La Jolla, CA 92093, USA

Author emails:
Allegra T. Aron - allegra.aron@du.edu

Author contributions:
A.T.A, M.R., and P.C.D. conceptualized the idea. A.T.A. performed LC-MS/MS analysis. A.K. performed analysis of metabolomics data; S.Z. performed analysis of whole genome sequencing data. K.M. and A.K. performed statistical analysis. H.Z. performed all animal work, and M.R. supervised animal work. A.K. and A.T.A. wrote the manuscript. All authors contributed to editing the manuscript.

Declaration of Interests:
PCD is an advisor and holds equity in Cybele and Sirenas and a Scientific co-founder, advisor and holds equity to Ometa, Enveda, and Arome with prior approval by UC-San Diego. PCD also consulted for DSM Animal Health in 2023.

SUMMARY

Iron is essential for life, but its imbalances can lead to severe health implications. Iron deficiency is the most common nutrient disorder worldwide, and iron disregulation in early life has been found to cause long-lasting behavioral, cognitive, and neural effects. However, little is known about the effects of dietary iron on gut microbiome function and metabolism. In this study, we sought to

investigate the impact of dietary iron on the fecal metabolome and microbiome by using mice fed with three diets with different iron content: an iron deficient, an iron sufficient (standard), and an iron overload diet for almost 7 weeks. Additionally, we sought to understand whether any observed changes would persist past the 7-week period of diet intervention. To assess this, all feeding groups were switched to a standard diet, and this feeding continued for an additional 7 weeks. Analysis of the fecal metabolome revealed that iron overload and deficiency significantly alter levels of peptides, nucleic acids, and lipids, including di- and tri-peptides containing branched-chain amino acids, inosine and guanosine, and several microbial conjugated bile acids. The observed changes in the fecal metabolome persist long after the switch back to a standard diet, with the cecal gut microbiota composition and function of each group distinct after the 7-week standard diet wash-out. Our results highlight the enduring metabolic consequences of nutritional imbalances, mediated by both host and gut microbiome, which persist after returning to original standard diets.

INTRODUCTION

Iron deficiency impacts more than two billion individuals worldwide, including ~40% of the population in the developing world and ~10% of the population in developed countries[1,2]. This makes it the most widespread nutritional deficiency across the globe. Deficiency of this essential metal can result in impaired immune response[3], stunted growth[4], and cognitive defects[5] due to the essential roles of iron in biological processes. These include erythropoiesis, oxygen transport, mitochondrial respiration, electron transfer/mediation of oxidation-reduction reactions, hormone synthesis, DNA replication, and cell cycle control[6]. Iron deficiency can occur during malnutrition[7] but is also observed in overnutrition[8,9]. Furthermore, iron homeostasis is altered in metabolic diseases like inflammatory bowel disease and non-alcoholic fatty liver disease[10], in neurodegenerative diseases like Alzheimer's and Parkinson’s diseases[11,12], and in cancers[13]. It is, therefore, essential to better understand how iron excess and deficiency can impact both host and microbial metabolism.

Nutrient availability profoundly shapes the composition and function of the microbial communities that colonize host organisms (humans, mice, etc.). This dynamic relationship is exceptionally relevant in the gut, where the levels of micronutrients, like polyphenols and flavonoids, or macronutrients, like carbohydrates and proteins, result in microbial communities with distinct compositions and functions[14,15]. Although underappreciated, metals, such as iron, copper, manganese, zinc, and cobalt, are also essential micronutrients required by all organisms and substantially influence the gut microbiota. Just as in higher organisms, iron is the most common redox-active metal found in enzymes[16] and is a critical component of both iron-sulfur clusters and heme, co-factors required for ATP production, detoxification of toxins, and mediating oxidation-reduction reactions. Given these important roles for iron, host organisms use iron sequestration to control the growth of pathogens in a process called nutritional immunity[17,18], yet metal acquisition pathways remain understudied in the context

of the commensal human microorganisms. For example, *Bacteroides thetaiotaomicron*, a human gut commensal bacterium, was recently found to use siderophores enterobactin and salmochelin produced by other bacteria to survive in the inflamed gut[19,20].

Little is known about how the gut microbiota acquires iron and how dietary iron levels affect the function of these organisms, though studies have shown that dietary iron levels modulate microbial composition[2,21]. For example, a decades-old study found higher counts of *Enterobacteriaceae* in infants receiving iron-fortified cow milk than in those receiving unfortified breast milk[22]. These results were reproduced in a study on the effects of dietary iron fortification in Kenyan infants, which also revealed increased levels of enterobacteria and decreased levels of lactobacilli[23]. These findings were dependent on diet, with a recent study showing that galacto-oligosaccharide/fructo-oligosaccharide prebiotics could modulate the gut microbiota toward a community rich in *Bifidobacterium* species[24]. Similar results have been observed in animal studies, with an increase in *Enterobacteriaceae* observed in both weaning pigs and rats fed iron-supplemented diets[23,25]. The study in rats investigated the effects of dietary iron deficiency and supplementation on short-chain fatty acid production but did not measure other metabolite levels.

While previous studies performed 16S rRNA sequencing to observe how changes in dietary iron levels affect gut microbiota composition, it remains unknown which enzymatic pathways of the gut microbial communities are modulated by these dietary changes[25]. Because of functional redundancy, where different microbial species encode for similar biological, untargeted metabolomics and metagenomic sequencing are essential to understanding the functional response of the gut microbiome to changing dietary iron. Previous human and animal studies investigating the metabolome under altered iron intake have focused on plasma, blood, and liver samples but effects on the fecal metabolome have been largely ignored[26–30]. Additionally, whether iron-mediated metabolic changes are reversible upon restoration of a standard diet remains an open question.

We performed a murine longitudinal study to address these knowledge gaps and assess whether dietary iron excess or deficiency can alter host and associated gut microbial metabolism in a way that persists past the dietary intervention period. Animals were assigned to one of three feeding groups: an iron deficient, an iron sufficient (standard), or an iron overload diet. Ferric citrate, a commonly used oral iron supplement and an approved food ingredient by various regulatory boards[31], was added to supplement an iron-deficient diet to standard or excess iron levels. This iron source has been previously demonstrated to affect fecal iron levels and the abundance of bacterial taxa in mice[32]. Moreover, it is well-established that elevated levels of dietary iron promote hepcidin signaling in the liver, leading to reduced iron absorption and accumulation in the intestinal lumen. Here, we investigate the impact of iron-deficient and overload diets on the fecal metabolome using untargeted liquid chromatography followed by tandem mass spectrometry (LC-MS/MS). All three feeding groups were then switched back to an iron-sufficient diet after 7 weeks of dietary intervention and

followed for an additional 7 weeks to assess whether observed changes could be reversed by restoring standard iron levels using LC-MS/MS and investigating cecal microbial communities using metagenomic sequencing.

RESULTS

The fecal metabolome is shaped by dietary iron level and converges when standard dietary iron levels are restored

To investigate whether dietary iron influences the metabolism of the host and the gut microbiome during development, mice between the ages of 30 and 36 days were divided into three feeding groups: a Fe-deficient group, a standard (Fe-sufficient) group, and a Fe-overload group. All 15 mice were initially fed a standard diet before the age of 5 weeks, (between 30 and 36 days). This point was defined as study day 0 when the adolescent mice were further divided into three groups and were provided with Fe-deficient, standard, or Fe-overload diets until study day 47. At this stage, all three feeding groups were switched back to the same standard diet (**Figure 1A**).

Our results show that the fecal metabolomes of the three diet groups begin diverging at the first point of collection on study day 4 and continue to diverge for the remainder of the dietary intervention period. Unsupervised principal component analysis (PCA) of the fecal metabolomes, along with permutational analysis of variance (PERMANOVA), was used to assess this separation (**Figure 1C**). The divergence between the three diet groups starts on day 4 (F = 3.7, p = 0.001) and continues to increase as time progresses past the day of the diet switch (F = 5.8, p = 0.002), reaching its maximum on day 61 (F = 8.4, p = 0.001). At the final two time points (days 82 and 96), the three groups begin to converge, revealing that, eventually, the differences in the fecal metabolic profiles diminish with time after iron levels are restored. Four PCA plots highlighting key time points in the study design are visualized in **Figure 1B**. These time points were taken immediately before the start of the dietary intervention (day 0), the conclusion of the intervention (day 47), the time point with maximal observed separation between groups (day 61), and the conclusion of the study (day 96).

No separation of metabolomic profiles is observed among the three diet groups on the initial day of the study (day 0). However, by the final day of the differential dietary iron intake intervention (day 47), separation is observed among the three feeding cohorts. While Fe-deficient and Fe-overload groups were switched back to standard, Fe-sufficient feed after day 47 fecal collection, the most significant difference between diet groups occurs at day 61 (**Figure 1B, Figure S1**). Finally, on day 96, the final time point for sample collection, the diet groups show obvious convergence of metabolic profiles. The full dataset was also subjected to unsupervised PCA analysis and colored by mouse individual and cage number metadata to confirm no significant clustering by individual mouse (**Figure S2A**), or by cage effect (**Figure S2B),** though a noticeable separation based on mouse age was observed (**Figure S2C**). Taken together,

unsupervised analysis suggests a strong relationship between dietary iron supplementation and the fecal metabolome of mice.

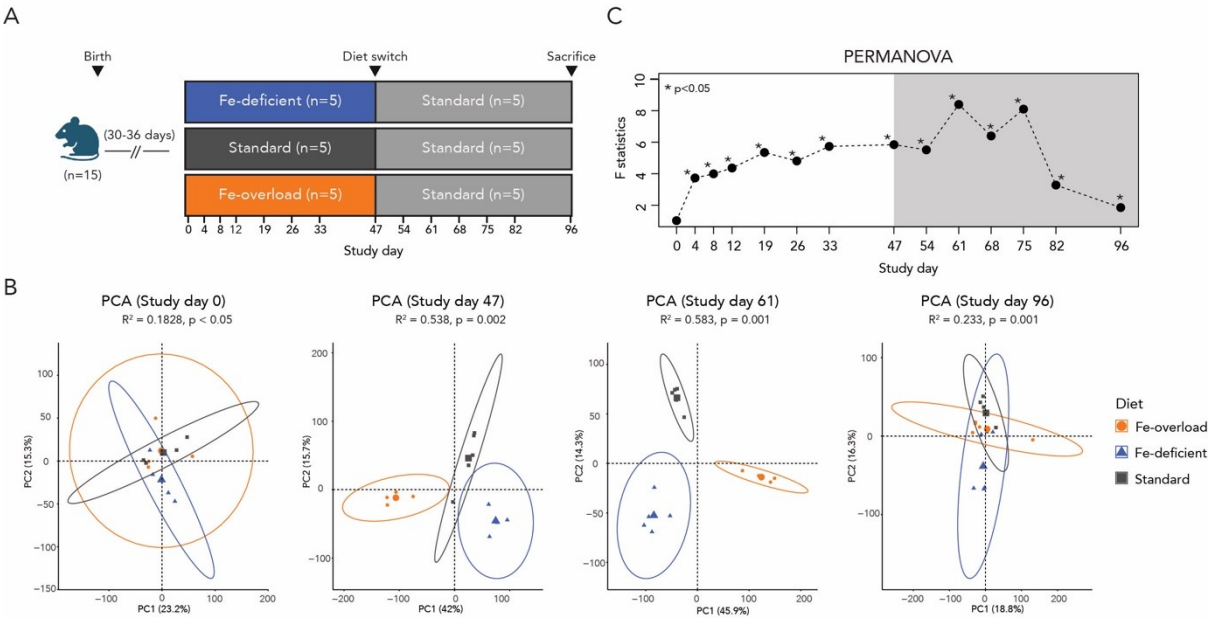

Figure 1. Dietary iron levels alter the fecal metabolome profile. (A) Design of the study. Mice were purchased from Jackson laboratory, and each diet cohort was housed separately in 2 cages per cohort. Days indicate fecal collection time points. The diet study was started at 30-36 days post-birth. (B) Unsupervised principal component analyses (PCAs) of the fecal metabolomes for days 0, 47, 61, and 96. Group centroids are included as a triangle and 95% confidence ellipses are included as visual aids. (C) Permutational analysis of variance (PERMANOVA) was calculated for each fecal collection timepoint in the study.

Differential dietary iron intake modulates lipid and peptide levels

To find metabolic features that differed between Fe-deficient, standard, and Fe-overload groups, pairwise partial least squares discriminant analysis (PLS-DA) was performed on the data collected on the final day of the dietary intervention (study day 47) (**Figure S3A-B**). This time point was chosen to represent the dietary intervention period as this day had the most pronounced metabolomic differentiation within the period before the washout (switch back to standard diet) based on PERMANOVA results. The features from study day 47 with the 30 highest PLS-DA loadings and VIP scores > 1 from pairwise PLS-DA for standard vs. Fe-deficient and standard vs. Fe-overload metabolomes were extracted and plotted (**Figure S3C-D**). Each feature was either paired to a level 2 annotation[33,34] using the Global Natural Products Social molecular networking platform (GNPS)[35] or using the *in silico* tools SIRIUS[36] and CANOPUS[37] to generate level 3 annotations[33,34]. In parallel, univariate statistical analysis was performed on study day 47 to corroborate the results of supervised multivariate analysis. Data from each diet group was checked separately for normality before univariate analysis (**Table S2**). One-way ANOVA was conducted on the three diet groups followed by a Tukey's post-hoc test to assess pairwise differences.

25 of the 30 features (83.3%) with the highest loading scores and VIP scores > 1 from pairwise PLS-DA of Fe-deficient versus standard diet were also significant in univariate analysis at day 47 (**Figure 2A**). The same percentage of features (25 of the 30, 83.3%) with the highest loading scores and VIP scores > 1 from pairwise PLS-DA of Fe-overload diet versus standard diet were also significant in univariate analysis (**Figure 2B)**. Overall, the agreement between the supervised multivariate and univariate results led us to further investigate molecular classes represented by the features driving the differences between the diet groups. Short asynchronous time-series analysis (SantaR)[38] was used to investigate the fluctuation of the features with high loading scores across the duration of the study (**Figure 2C**). While some features were exclusively present in one diet group (oligopeptides in Fe-deficient diet, medium-chain fatty acids and purine nucleosides/tides in Fe-overload diet), other features were suppressed in only one diet, such as the methylpyridine family of metabolites in the case of Fe-overload. The temporal dynamics also differed based on feature; for example, some features exhibited differences immediately on study day 4 (i.e., medium-chain fatty acid), while others showed longer delays in response (i.e., oligopeptide production). Using this analysis, we were able to prioritize molecular classes that were most impacted by dietary iron for further analysis.

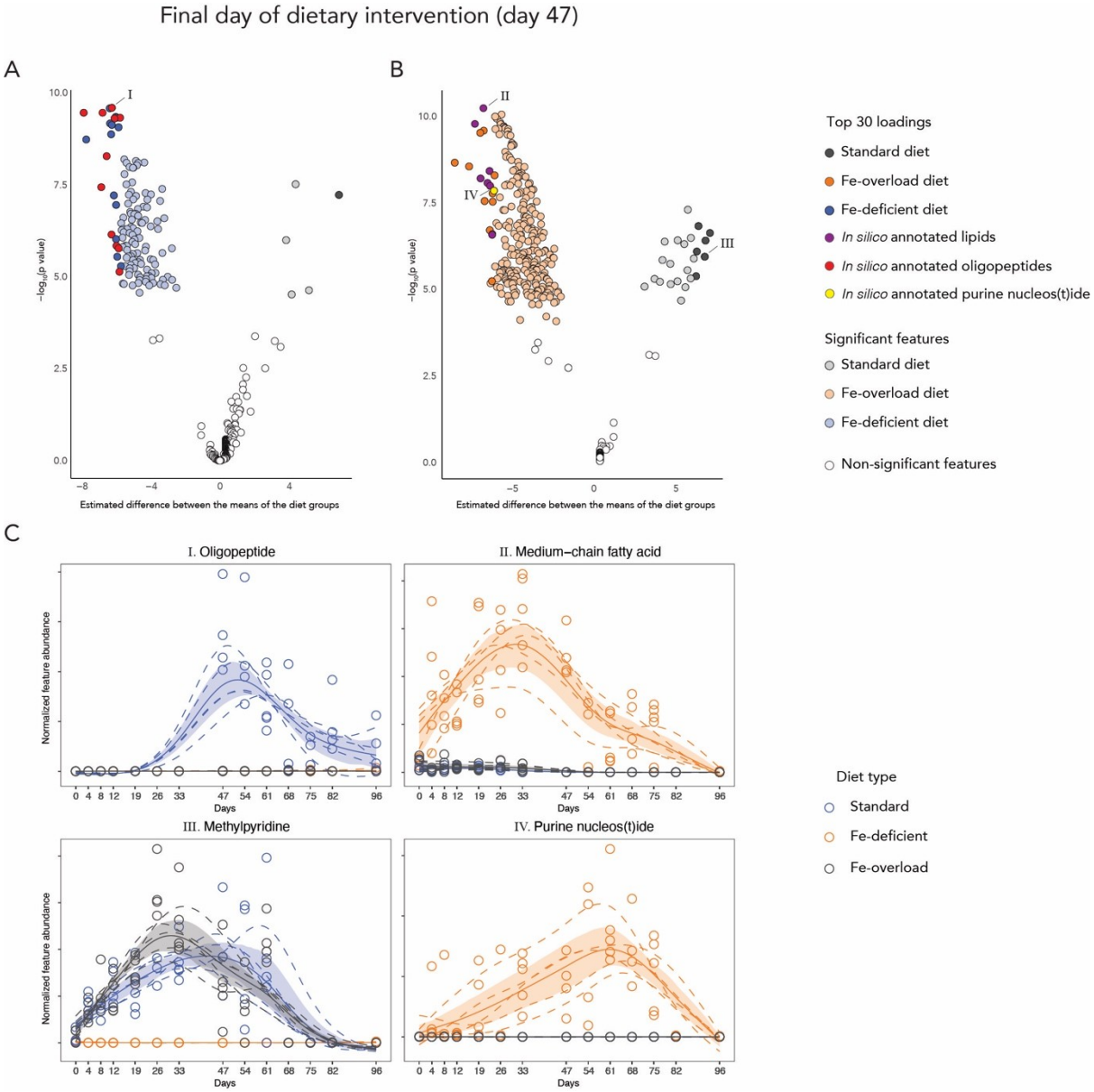

Figure 2. Oligopeptide, lipid, purine nucleoside, and methylpyridine molecular families are modulated by dietary iron level. (A) Univariate analysis comparing standard and Fe-deficient diets show consistency with the supervised approach, as the 30 highest loadings are also significant features in univariate analyses. 11 out of 30 features extracted from PLS-DA are representative of oligopeptide molecular class. (B) Univariate analysis for standard vs Fe-overload diets highlights presence of lipid molecules (mostly fatty-acids and derivatives; 7 out of 30) and purine nucleos(t)ide molecule in Fe-overload case. (C) Representative short asynchronous time-series analysis plots changes in mean abundance over the time course study for select significant features. Short asynchronous time-series analysis plots were generated using normalized feature abundances.

Metabolism eventually recovers from exposure

To assess the persistence of observed metabolic changes for select molecular classes, we applied this approach to the dataset from samples collected on study day 61, when the highest separation of metabolic profiles between three diets

was observed. Similarly, the top 30 features with the highest loadings and VIP scores > 1 were extracted from each pairwise PLS-DA model, comparing Fe-deficient versus standard diets and Fe-overload versus standard diets **(Figure S4).** The significance of extracted loadings was juxtaposed with the results of univariate analysis for the study day 61. Notably, 26 out of 30 features (86.7%) exhibited significance in the univariate analysis for the Fe-deficient and standard diet comparison (**Figure 3A**). 12 out of 30 features (40.0 %) of differential loadings were significant for Fe-overload and standard diets (**Figure 3B**). Upon annotating these features with level 2 and level 3 confidence levels, consistent molecular class trends surfaced, resembling those observed during the dietary intervention period. Specifically, a heightened presence of oligopeptides was noted in the Fe-deficient diet compared to the standard group, while increased levels of fatty acids were evident in the Fe-overload group. Significantly, a substantial proportion of the metabolic changes induced by varying dietary iron loads persisted beyond the differential diet period, extending into the washout period. Moreover, in the majority of these instances, the altered levels of molecule production were restored upon reverting to a standard diet. This underscores the resilience and reversibility of the metabolic effects associated with different dietary iron loadings.

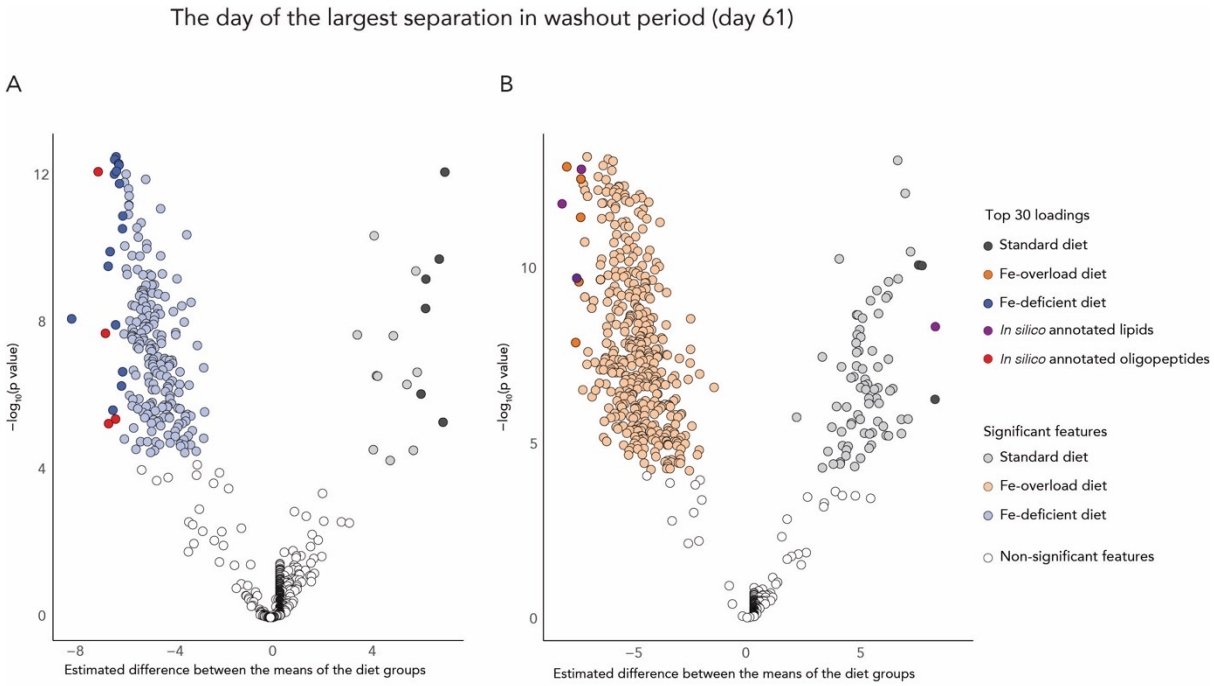

Figure 3. Differential abundance features persist into the washout phase before eventually recovering. Univariate analysis shows consistency with the supervised multivariate approach, as the 30 highest loading features are also significant features in the univariate analysis of Fe-deficient versus standard diets (A) and Fe-overload versus standard diets (B).

Fe-deficiency diet results in fecal di-, tri-, and oligopeptides increased abundance

Feature-based molecular networking (FBMN) was performed in GNPS on the full dataset across all days of collection and visualized in Cytoscape 3.9.1[39]. The color composition of the pie charts corresponds to the specific diet type cohorts in which the molecule was detected. In total, 6687 features were detected after blank subtraction, and among them, 374 were annotated in GNPS to yield a 6.5% annotation rate. Features were grouped by MS/MS spectral similarity, facilitating the organization of the large dataset obtained from the experiment. Visual assessment of the molecular network colored by diet metadata (**Figure S5**) revealed that networks containing at least one annotated peptide member were predominantly present in the Fe-deficient diet samples, highlighted in red. Moreover, given that numerous features with high predictive power for the Fe-deficient diet were annotated as peptides using *in silico* methods, we further investigated this molecular class.

More than 20 features could be annotated as level 2 matches[33,34] to peptide library spectra in GNPS, with annotations concentrated as di- and tri-peptides. Clear hierarchical clustering patterns emerge when heatmaps for annotated peptides were constructed (**Figure S7**), with peptides exhibiting substantially higher abundance in Fe-deficient samples than in the other two dietary conditions. Notably, samples with the highest peptide abundance were collected during the later days of the study (study days 68 and 75), as visualized in the short asynchronous time-series analysis (**Figure 4A**).

Peptides consistently exhibited distinct profiles for the Fe-deficient diet compared to the other two diets. Peptide abundance increased at study day 33 and peaked around study day 68 before gradually returning to low levels that matched the standard diet (**Figures 4A** and **S6**). This observation is intriguing for several reasons: first, the change in peptide profiling is reversible once iron is reintroduced into the deficient diet; and second, there appears to be a delay between the diet switch and the response in peptide abundance to this change. As with the level 2 peptide annotations, the same trend was also observed for the 743 features with *in silico* di- and tri-peptide annotations (**Figure S8**). Heatmaps revealed a robust hierarchical clustering pattern, along with increased abundance in the Fe-deficient samples for most of these features during the later timepoints (**Figures S7** and **S8**).

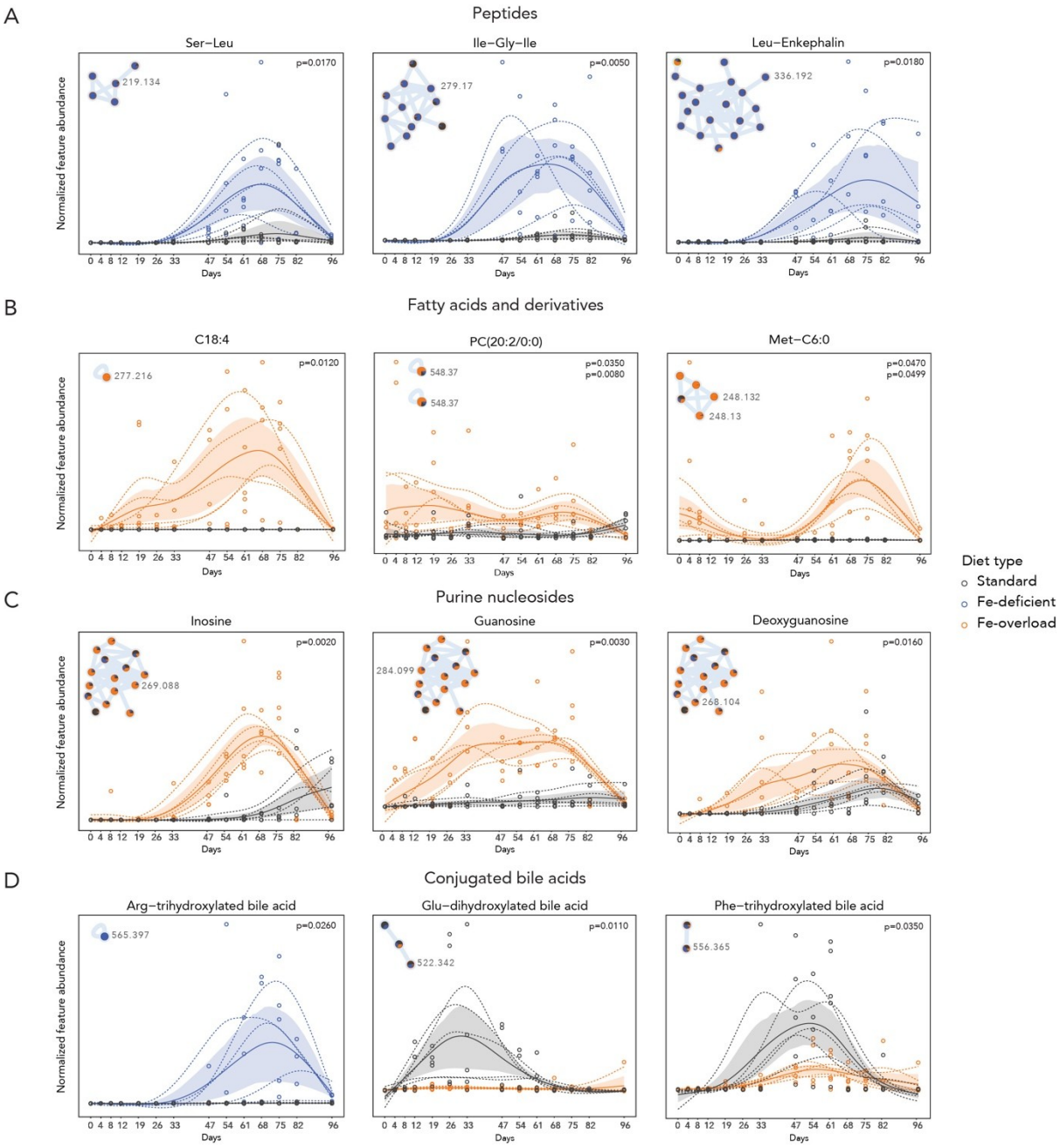

Figure 4. Short asynchronous time-series analysis of molecular features modulated by dietary iron. Normalized feature abundance was plotted as a time course analysis over all days of the diet study for the following molecular classes: (A) peptides, (B) fatty acids and derivatives, (C) purine nucleosides, and (D) conjugated bile acids. These molecular classes were prioritized based on numerous instances within features found with VIP scores > 1 and high loadings. Each plot is constructed for the comparison of two diet types (Fe-deficient vs. standard and Fe-overload vs. standard). Feature abundance for the omitted diet type matches the trend in the standard diet. Plots visualizing all three diet types at a time can be found in the Supplementary Information. The inset of each plot represents the molecular network to which the feature belongs and was retrieved from GNPS and visualized in Cytoscape.

Fe-overload diet results in increased fecal abundance of fatty acid derivatives and purine nucleosides

While di- and tripeptides were found to differentiate between standard and Fe-deficient diets, 13 of the 30 VIP features from PLS-DA of Fe-overload versus standard diet are fatty acids and derivatives. Stearidonic acid and methionine-conjugated caproic acid level 2 annotations (**Figure 4B**) were among the features with increased abundance in Fe-overload. In both cases, the highest abundance was observed after the diet switch then decreased to levels present in the standard diet by study day 96. Several additional phospholipids, including specific lysophosphatidylcholines, exhibited distinct profiles in the Fe-overload diet. At the same time, certain phosphatidylethanolamine molecules were abundant in both standard and Fe-deficient diets but were below the limit of detection in the Fe-overload diet. Distinct clustering of Fe-overload diet and Fe-deficient diet samples were also observed in heatmaps constructed for *in silico* annotated lipids (**Figure S10**).

Along with fatty acids and their derivatives, purine nucleosides were also increased in abundance in the Fe-overload diet with respect to standard and Fe-deficient diets. Specifically, inosine, guanosine, and deoxyguanosine level 2 annotations were more abundant in Fe-overload (**Figure 4C**). After the diet switch back to standard, all three molecules converged back to levels in the standard diet. This points to the reversibility of the iron-dependent increases in abundance. While the abundance of inosine in the Fe-overload diet began to increase on study day 33 of sample collection and peaked around study days 61-68, it eventually returned to levels matching those observed in the standard diet by the conclusion of the study (**Figure 4C**). In contrast, increases in guanosine and deoxyguanosine abundance started earlier (day 4 for guanosine and day 19 for deoxyguanosine). Enrichment of guanosine and deoxyguanosine was consistently observed throughout most of the study period, even after the return to a standard diet, and only began to decrease on day 75. When the *in silico* annotated purine nucleosides and nucleotides (based on NPC class[40], ClassyFire most specific class, and ClassyFire class annotations[41]) were clustered into a heatmap, Fe-overload samples exhibit a similar trend in the purine nucleoside abundance profiles (**Figure S12**).

Iron intake levels differentially influence microbial metabolite production

While peptides, fatty acid derivatives, and purine nucleosides can be produced by both host and the gut microbiota, amino acid-conjugated bile acids[42–44] are produced exclusively by microbial communities[42–44]. This class of bile acids conjugates was also found to be influenced by dietary Fe levels. More broadly, bile acid homeostasis was altered in both Fe-overload and Fe-deficiency (**Figure S14**). This finding was consistent with previous reports showing that Fe-overload in rats altered bile acid homeostasis through altered enzyme expression[45]. In addition to the host-produced bile acids reported previously, we found twelve of the 39 total spectral matches to conjugated bile acids were affected by differential iron supplementation (**Figure S13**). Of these, 9 trihydroxylated bile acids were found to be differentially abundant between the diets. These were primarily conjugated with aromatic and heterocyclic amino acids, including

phenylalanine (Phe), tryptophan (Trp), tyrosine (Tyr), and histidine (His), as well as non-polar isoleucine and leucine (Ile/Leu), and polar threonine (Thr). The remaining three spectral matches were to recently discovered dihydroxylated bile acid conjugates, specifically conjugated to threonine (Thr), glutamate (Glu), and histidine (His)[42–44,46]. While the distribution pattern of each conjugated bile acid varies, most detected bile acid conjugates exhibited reduced abundance in dietary Fe-overload compared to standard and Fe-deficient diets. An arginine-conjugated trihydroxylated bile acid was the only bile acid conjugate to exhibit a remarkably different trend, with a higher abundance in the Fe-deficient diet than in both standard and Fe-overload diets[47]. The abundance of this feature increased after the diet switch but reverted to standard diet levels by the end of the study.

Iron intake influences cecal microbiome composition and function

The metabolic profiles exhibit a lag between the conclusion of differential dietary Fe feeding (study day 47) and the day of maximal separation between groups through PCA (study day 61). Moreover, while the group separation decreases after study day 61 to study day 96, after the removal of the iron imbalance in their diet, there remains significant separation between the original diet groups at study day 96 (PERMANOVA R^2 = 0.233, p= 0.001). We hypothesized that this persistence in the fecal metabolome difference was a result of changes in gut microbiota composition and functionality that took place alongside changes in host metabolism. To investigate this hypothesis, metagenomic sequencing was performed on cecal samples collected at the end of the study (study day 96). Unsupervised PCA analysis of metagenomic data was consistent with this hypothesis, revealing significant separation between groups based on microbial composition (R^2=0.24, p=0.014) at the study conclusion (**Figure 5A** and **5C**). Supervised PLS-DA confirmed unsupervised results, and differential abundance analysis using ALDEx2 was used to identify signature taxa and (**Figure 5B** and **5D**). The microbial taxa driving separations between the standard diet group and the Fe-deficient group were consistent with previously reported changes in literature. For example, both the *Lactobacillus* and *Limosilactobacillus* genera were increased in abundance during iron deficiency. This is consistent with previous reports that *Limosilactobacillus* and *Lactobacillus* both facilitate iron absorption during anemia[48–50]. On the other hand, taxa observed in higher abundance in the Fe-overload group have been previously associated with dysbiosis, such as *Anaerotruncus colihominis*[51], and high Fe-levels, like *Blautia* and *Ruminococcacae*[52].

In addition to the altered cecal microbial composition, differences in enzyme profiles between the diet groups were also observed. Differentially abundant enzymes with an effect size >2 were further investigated. Interestingly, almost all enzymes were downregulated in cases of abnormal iron loading (both Fe-overload and Fe-deficiency) as compared to standard diet. Overall, the expression of 44 enzymes was decreased in the Fe-deficient group compared to the standard one (**Figure 5F**), while the expression of 39 enzymes was decreased and 1 was increased in mice fed an Fe-overload as compared to a

standard diet (**Figure 5G**). Of these, the expression of 22 enzymes was affected in both the Fe-deficient and Fe-overload groups.

The KEGG Mapper prediction tool[53,54] was utilized to identify the pathways affected by altered dietary iron levels. Biosynthesis of secondary metabolites was the most affected pathway with the expression of 14 enzymes altered in this pathway. 5 enzymes in the purine metabolism pathway were also found to be suppressed in both Fe-deficient and Fe-overload conditions as compared to standard. Decreased expression of an additional enzyme (phosphoribosylglycinamide formyltransferase 1) was observed in Fe-deficiency as well as in Fe-overload (amidophosphoribosyltransferase). *De novo* purine biosynthesis was most affected by the modulation of dietary iron (**Figure S17**), as the activity of key enzymes is iron-dependent. Five additional translocase enzymes linked to the hydrolysis of nucleoside triphosphates were also modulated by dietary iron. This observation is consistent with iron-dependent changes in purine nucleoside abundance observed in fecal metabolomics data (**Figure 4C** and **Figure S11**).

Branched-chain amino acid (BCAA) biosynthesis was suppressed in the Fe-deficient diet, and to a lesser degree, in Fe-overload diets (**Figure S18**). Specifically, enzymes responsible for the first and third steps of BCAA biosynthesis, acetohydroxyacid synthase and dihydroxy-acid dehydratase (DHAD), respectively, show high effect sizes in the Fe-deficient diet and less pronounced effects in the Fe-overload diet. DHAD contains two active-site Fe–S clusters that are likely modulated by iron availability[55–58]. In addition to BCAA biosynthesis, alanine (Ala), aspartate (Asp), and Glu biosynthesis, Phe, Tyr, and Trp biosynthesis along with Arg biosynthesis were decreased in both Fe-deficient and Fe-overload groups (**Figure S19**, **S20**, **S21**), while ornithine biosynthesis was specifically perturbed in the Fe-overload diet (**Figure S20**). Fatty acid and polyunsaturated fatty acid biosynthesis was affected in the Fe-deficient diet versus the standard diet. The gene encoding 3-oxoacyl-[acyl-carrier-protein] reductase was found at significantly lower levels in Fe-deficient cohort compared to a standard diet. Altered lipid biosynthesis is consistent with metabolomics data, which revealed increased levels of fatty acids and PCs in Fe-overload diet as compared to Fe-deficient and standard diets (**Figure S22**). We consistently observe decreased enzyme expression of those enzymes containing Fe-S clusters.

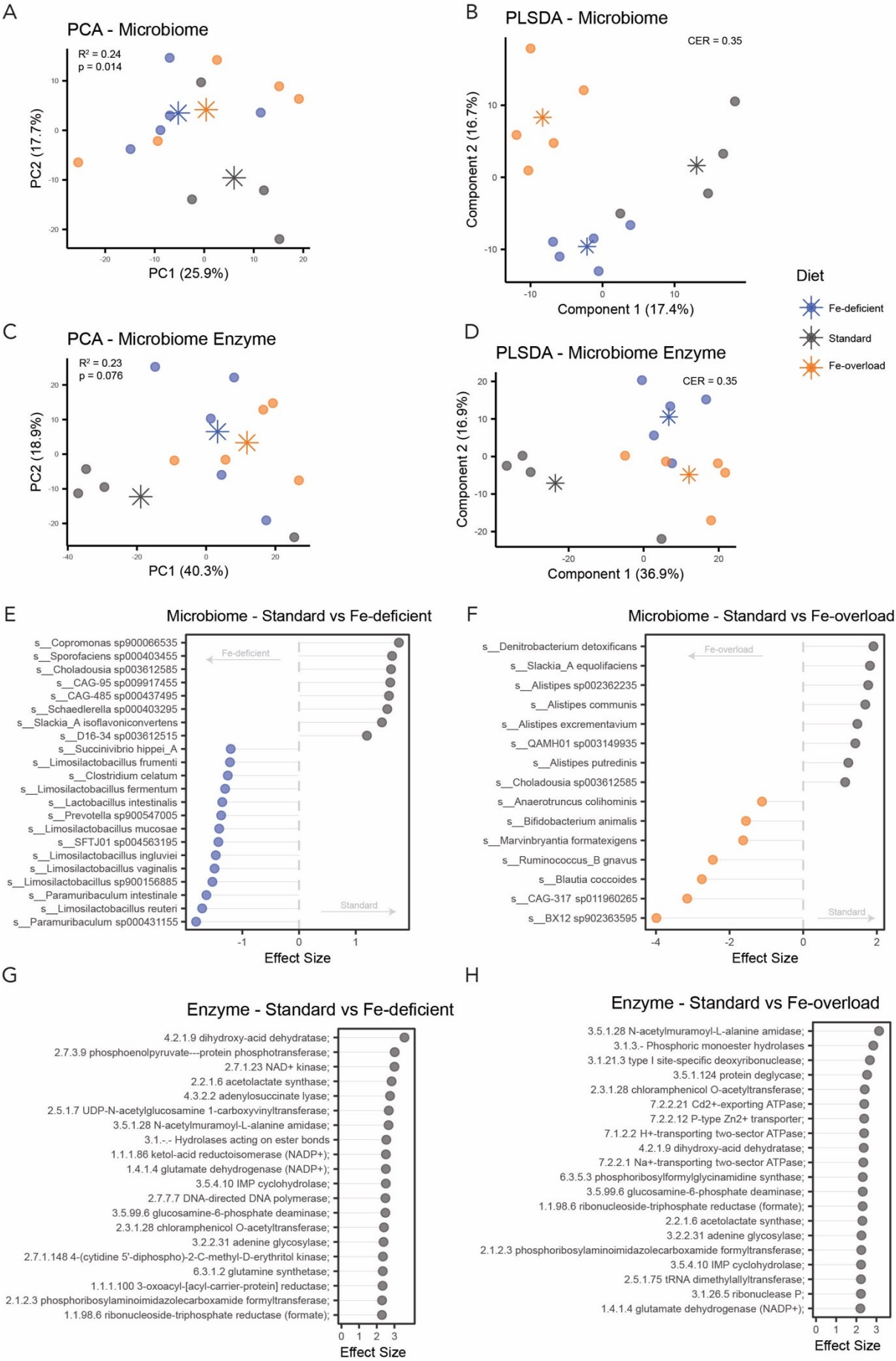
A
PCA - Microbiome
R² = 0.24
p = 0.014
PC2 (17.7%)
PC1 (25.9%)
B
PLSDA - Microbiome
CER = 0.35
Component 2 (16.7%)
Component 1 (17.4%)
Diet
Fe-deficient
Standard
Fe-overload
C
PCA - Microbiome Enzyme
R² = 0.23
p = 0.076
PC2 (18.9%)
PC1 (40.3%)
D
PLSDA - Microbiome Enzyme
CER = 0.35
Component 2 (16.9%)
Component 1 (36.9%)
E
Microbiome - Standard vs Fe-deficient
s__Copromonas sp900066535
s__Sporofaciens sp000403455
s__Choladousia sp003612585
s__CAG-95 sp009917455
s__CAG-485 sp000437495
s__Schaedlerella sp000403295
s__Slackia_A isoflavoniconvertens
s__D16-34 sp003612515
s__Succinivibrio hippei_A
s__Limosilactobacillus frumenti
s__Clostridium celatum
s__Limosilactobacillus fermentum
s__Lactobacillus intestinalis
s__Prevotella sp900547005
s__Limosilactobacillus mucosae
s__SFTJ01 sp004563195
s__Limosilactobacillus ingluviei
s__Limosilactobacillus vaginalis
s__Limosilactobacillus sp900156885
s__Paramuribaculum intestinale
s__Limosilactobacillus reuteri
s__Paramuribaculum sp000431155
Fe-deficient
Standard
Effect Size
F
Microbiome - Standard vs Fe-overload
s__Denitrobacterium detoxificans
s__Slackia_A equolifaciens
s__Alistipes sp002362235
s__Alistipes communis
s__Alistipes excrementavium
s__QAMH01 sp003149935
s__Alistipes putredinis
s__Choladousia sp003612585
s__Anaerotruncus colihominis
s__Bifidobacterium animalis
s__Marvinbryantia formatexigens
s__Ruminococcus_B gnavus
s__Blautia coccoides
s__CAG-317 sp011960265
s__BX12 sp902363595
Fe-overload
Standard
Effect Size
G
Enzyme - Standard vs Fe-deficient
4.2.1.9 dihydroxy-acid dehydratase;
2.7.3.9 phosphoenolpyruvate---protein phosphotransferase;
2.7.1.23 NAD+ kinase;
2.2.1.6 acetolactate synthase;
4.3.2.2 adenylosuccinate lyase;
2.5.1.7 UDP-N-acetylglucosamine 1-carboxyvinyltransferase;
3.5.1.28 N-acetylmuramoyl-L-alanine amidase;
3.1.-.- Hydrolases acting on ester bonds
1.1.1.86 ketol-acid reductoisomerase (NADP+);
1.4.1.4 glutamate dehydrogenase (NADP+);
3.5.4.10 IMP cyclohydrolase;
2.7.7.7 DNA-directed DNA polymerase;
3.5.99.6 glucosamine-6-phosphate deaminase;
2.3.1.28 chloramphenicol O-acetyltransferase;
3.2.2.31 adenine glycosylase;
2.7.1.148 4-(cytidine 5'-diphospho)-2-C-methyl-D-erythritol kinase;
6.3.1.2 glutamine synthetase;
1.1.1.100 3-oxoacyl-[acyl-carrier-protein] reductase;
2.1.2.3 phosphoribosylaminoimidazolecarboxamide formyltransferase;
1.1.98.6 ribonucleoside-triphosphate reductase (formate);
Effect Size
H
Enzyme - Standard vs Fe-overload
3.5.1.28 N-acetylmuramoyl-L-alanine amidase;
3.1.3.- Phosphoric monoester hydrolases
3.1.21.3 type I site-specific deoxyribonuclease;
3.5.1.124 protein deglycase;
2.3.1.28 chloramphenicol O-acetyltransferase;
7.2.2.21 Cd2+-exporting ATPase;
7.2.2.12 P-type Zn2+ transporter;
7.1.2.2 H+-transporting two-sector ATPase;
4.2.1.9 dihydroxy-acid dehydratase;
7.2.2.1 Na+-transporting two-sector ATPase;
6.3.5.3 phosphoribosylformylglycinamidine synthase;
3.5.99.6 glucosamine-6-phosphate deaminase;
1.1.98.6 ribonucleoside-triphosphate reductase (formate);
2.2.1.6 acetolactate synthase;
3.2.2.31 adenine glycosylase;
2.1.2.3 phosphoribosylaminoimidazolecarboxamide formyltransferase;
3.5.4.10 IMP cyclohydrolase;
2.5.1.75 tRNA dimethylallyltransferase;
3.1.26.5 ribonuclease P;
1.4.1.4 glutamate dehydrogenase (NADP+);
Effect Size

Figure 5. Dietary iron levels significantly alter cecal microbiome composition and functionality. (A) Unsupervised principal component analysis (PCA) reveals separation between the three study groups after the study (day 96) according to PERMANOVA (R^2 = 0.024, p= 0.014). (B) PLS-DA of cecal microbial communities between the three study groups. (C) PCA reveals separation within enzyme function at the conclusion of the diet study and switch back to normal feeding (R^2 = 0.023, p= 0.076). (D) PLS-DA of microbial enzymatic function between the three study groups. Group centroids are included as a triangle along with 95% confidence ellipticals as visual aids. ALDEx2 differential abundance analysis identified taxa signatures of (E) Fe-deficient vs standard groups and (F) standard and Fe-overload groups and enzymatic signatures of (G) Fe-deficient and standard groups and (H) Fe-overload and standard groups.

DISCUSSION

Differential dietary iron intake affected the fecal metabolome throughout the dietary study. Cecal microbiome composition and function were only assessed at the completion of the study, at which point composition and function differed by dietary group. Observed changes in the metabolome and microbiome persisted for 49 more days past the end of dietary intervention after Fe-deficient and Fe-overload feeding groups were switched back to a standard diet. These findings highlight the importance of dietary iron on both host and microbial metabolism and microbiome composition. The differential iron feeding altered levels of peptides, nucleic acids, and lipids (fatty acid and bile acid) metabolism and persisted even long after diets were reverted to standard iron intake.

These molecular classes were also consistent with Fe-dependent modulation of enzyme expression. For example, nearly half of the top 30 features with the highest loadings and VIP scores > 1 from pairwise PLS-DA between Fe-deficient and standard diets for the dietary intervention period were di- or tripeptides (**Figure 2A**), and the expression of enzymes involved in BCAA, Arg, Ala, Asp, and Glu metabolism was decreased in Fe-deficiency. These results indicate that the gene expression of enzymes responsible for BCAA biosynthesis was suppressed, thereby reducing *de novo* synthesis of amino acids. BCAAs can only be synthesized by bacteria and fungi but not animals[59], so reduced microbiome BCAA biosynthesis may be consistent with the prominent increases in di- and tri-peptides containing branched-chain amino acids that are observed in the Fe-deficient group as compared to the standard diet (**Figure S7**). We speculate that protein catabolism by either the host or the gut microbiota may be responsible for the observed increase in di- and tripeptides as a compensatory mechanism for reduced biosynthesis.

Amongst the the top 30 features with the highest loadings and VIP scores > 1 from the pairwise PLS-DA of Fe-overload and standard diets were mostly lipids (including both mono-, di-, and tri-carboxylic acids and bile acids) and nucleic acids. As in the Fe-deficient versus standard pairwise comparison, the modulated metabolome features between Fe-overload versus standard diet groups were consistent with altered enzyme expression at the study conclusion. For example, 6 enzymes in the purine metabolism pathway were suppressed in the Fe-

overload group (**Figure S17**), likely due to the iron dependence of key enzymes in this pathway. For example, the activity of ribonucleotide reductase (RNR), an enzyme essential for DNA synthesis and repair, depends on iron in its active site [4Fe-4S] cluster[60–62]. Enzymes participating in purine salvage, such as adenylosuccinate lyase (ADSL), also exhibit iron-dependent activity, with ADSL levels elevated in the liver of nursing piglets fed a high-iron diet[63].

Purine metabolites produced by both the host and gut microbiota serve as critical messengers beyond their canonical functions in DNA and RNA, and the gut microbial communities play a crucial role in modulating purine nucleoside levels[64]. Disruption of purinergic signaling has been linked to health conditions ranging from inflammation and neurodegeneration to cancer[65], as purines are crucial building blocks for nucleotides used by intestinal mucosa for immunity, energy production, and cell growth[66]. Moreover, increased purine salvage, triggered by the elevated degradation of purine nucleotides by both the host and the gut microbiota, has been described as contributing to inflammatory bowel disease[67], while gut bacterial purine catabolism may be a key mechanism driving atherosclerosis through the modulation of uric acid levels[68]. Consistent with this study, Fe-dependent modulation of purine metabolism was observed previously in liver and hippocampus metabolomes in a nursing piglet model; upon dietary Fe-overload treatment, guanosine, inosine, and other purine metabolites were detected to suggest a shift in flux from the salvage pathway toward degradation[63]. The present study provides the first evidence of the impact of dietary Fe on purine nucleosides in fecal samples, suggesting that dietary Fe affects a key aspect of gut microbiota-host signaling.

Bile acids have also recently emerged as important signaling molecules in the host that act through receptor binding[43,69]. Fe-overload in rats was previously demonstrated to alter bile acid homeostasis through reduced expression of Cyp7a1, the enzyme that performs the rate-limiting conversion of cholesterol into cholic acid, and decreased expression of Bsep, the transporter responsible for bile acid efflux[45]. This study was consistent with this previous report, as bile acid homeostasis was altered in both Fe-overload and Fe-deficient diet groups as compared to the standard diet group (**Figure S14**). We were intrigued to find that amino acid conjugated bile acids[43] were also modulated by dietary Fe levels. While recently discovered in biological samples, these molecules have reported bioactivities ranging from protection against the deleterious effects of high-fat diets[70] to antagonizing the farnesoid X receptor (FXR)[42,71]. Different conjugated bile acids exhibit specific patterns in Fe-deficient or Fe-supplemented diets as compared to standard diets. For example, Arg-bMCA increased during Fe-deficiency relative to the standard diet, while Glu-CDCA increased in the standard diet relative to Fe-overload (**Figure 4D**). As unique microorganisms can produce each bile acid conjugate[41,68], we hypothesize that the different microbial taxa within each diet group result in a characteristic conjugated bile acid signature.

In conclusion, this is the first study demonstrating the role of dietary Fe in modulating both host and microbial metabolites in fecal samples. Importantly,

this study also suggests that while many metabolites exhibit reversible abundance profiles when animals return to a standard diet, the gut microbiota composition and function remain divergent between the different diet groups even after a long wash-out period.

LIMITATIONS OF THE STUDY

All MS/MS spectral matches are level 2 or 3 annotations, meaning that stereochemistry and regiochemistry may remain undefined. Additionally, a retention time drift of approximately 14 seconds was observed for the internal standard (**Figure S15**), and although our feature finding in MZmine was set with a retention tolerance that takes this drift into account, there remain some split features. All spectral annotations with more than one match were manually inspected, and any split features (observed in MZmine) were summed. In these cases, this is explicitly stated.

METHODS

Animals. Wild-type specific pathogen-free C57BL/6 mice were purchased from the Jackson Laboratory and used in our study, under protocols and guidelines approved by the Institutional Animal Care and Use Committee of the University of California, San Diego. Overall, each diet cohort contained 5 mice housed in two cages per cohort, with 2-3 mice per cage. In the normal and Fe-overload diet cohorts, there were 5 female mice housed in 2 cages per group. The Fe-deficient diet was fed to two male mice and three female mice housed in 2 separate cages.

Dietary intervention. The following diets were used in the study. (1) Iron deficiency: Teklad diet, TD.120514; (2) Standard iron: in Teklad diet, TD.120515, 50 ppm ferrous sulfate was replaced with ferric citrate; (3) Iron overload: Teklad diet, TD.120514, 6 g of ferric citrate iron/kg of diet (6000 ppm iron) were added.

Sample Collection. Fecal pellets were collected on days 0, 4, 8, 12, 19, 26, 33, 40, 47, 54, 61, 68, 75, 82, and 96. Mice were sacrificed on day 96 and organs were collected under sterile conditions.

Sample Processing for MS. Fecal samples were thawed on ice for 30 mins before adding a stainless-steel bead to every sample. 80% MeOH solvent was added to each sample to maintain mass-to-volume ratio of 1 mg per 10 µL. Samples were homogenized at 25 Hz for 5 min, centrifuged at max speed for 15 min, then supernatant was transferred and dried in vacuo overnight. Samples were stored at -80 °C until analysis, at which point they were reconstituted in 80% MeOH+1uM sulfadimethoxine to 1 mg/mL.

UHPLC-MS/MS. For LC-MS/MS analysis, 5 µL were injected into a Vanquish UHPLC system coupled to a Q-Exactive orbitrap mass spectrometer (Thermo Fisher

Scientific, Bremen, Germany). For the chromatographic separation, a C18 porous core column (Kinetex C18, 50 x 1.0 mm, 1.8 um particle size, 100 A pore size, Phenomenex, Torrance, USA) was used. For gradient elution, a high-pressure binary gradient system was used. The mobile phase consisted of solvent A H_2O + 0.1 % formic acid (FA) and solvent B acetonitrile (ACN) + 0.1 % FA. The flow rate was set to 0.15 mL/min. After injection, the samples were eluted with one of the following linear gradients: 0-1 min, 5% B, 1-7 min 5-99% B, followed by a 2.5 min washout phase at 99% B and a 1.5 min re-equilibration phase at 5% B. Data dependent acquisition (DDA) of MS/MS spectra was performed in positive mode. Electrospray ionization (ESI) parameters were set to 40 L/min sheath gas flow, 14 L/min auxiliary gas flow, 0 L/min sweep gas flow and 400°C auxiliary gas temperature; the spray voltage was set to 3.5 kV and the inlet capillary to 320°C and 50 V S-lens level was applied. MS scan range was set to 150-1500 m/z with a resolution at m/z 200 ($R_{m/z\ 200}$) of 35,000 with one micro-scan. The maximum ion injection time was set to 100 ms with an automated gain control (AGC) target of 1.0E6. Up to 5 MS/MS spectra per MS1 survey scan were recorded DDA mode with $R_{m/z\ 200}$ of 17,500 with one micro-scan. The maximum ion injection time for MS/MS scans was set to 100 ms with an AGC target of 5E5 ions. The MS/MS precursor isolation window was set to m/z 1. Normalized collision energy was set to a stepwise increase from 20 to 30 to 40% with z = 1 as default charge state. MS/MS scans were triggered at the apex of chromatographic peaks within 2 to 15 s from their first occurrence. Dynamic precursor exclusion was set to 5 s. Ions with unassigned charge states were excluded from MS/MS acquisition as well as isotope peaks.

Feature Finding and Molecular Networking. Raw data conversion to mzML format and peak picking were performed using MSConvert and MZmine. Both .raw and .mzML files were uploaded to MASSIVE database and made available for public access (ftp://massive.ucsd.edu/MSV000084783/). Data processing was carried out in MZmine 3.4[72] using the parameters specified in the .xml batch file in the Supplementary Information. Subsequently, feature based molecular networking (FBMN) was performed in the GNPS platform using the .mgf file and feature table retrieved from MZmine 3.4, along with the metadata file. Bray-Curtis PCoA Distance Metric and row sum normalization were applied to the GNPS job. The GNPS job link can be found here: https://gnps.ucsd.edu/ProteoSAFe/status.jsp?task=d35b583c2cf3435289a0aca8de4df4dd.

Statistical Analysis. The mass spectrometry data were further processed in the statistical software environment R (version 4.1.2). The MZmine feature table was blank subtracted with a cutoff value of 0.3 (i.e., features with a ratio of mean intensity in blanks vs mean intensity of features less than 30% were considered background noise and removed). After blank subtraction, minimum LOD (Limit of Detection) imputation was applied. The imputed data table was then either normalized by total ion count per sample or was subjected to centered log-ratio (CLR) transformation using the vegan 2.6.4 package. The imputed, normalized

data were used in short asynchronous time-series analysis, while the CLR-scaled feature table was utilized in subsequent univariate and multivariate analyses.

For the univariate analysis, the processed feature table was merged with the metadata table and checked for normality using the Shapiro-Wilk test. Due to the interest in the pairwise comparison of abnormal Fe loadings to standard dietary levels, we divided the data into different sets based on diet types and time: Standard & Fe-overload before the diet intervention, Standard & Fe-deficient before the diet intervention, Standard & Fe-overload after the wash-out, Standard & Fe-deficient after the wash-out. The majority of features in every dataset were found to be normally distributed. Therefore, an ANOVA test was performed on each feature against the sample area followed by the Tukey HSD post-hoc test to evaluate the differences among different diets at a significance level of $p < 0.05$.

Unsupervised principal component analysis (PCA) and supervised partial least squares-discriminant analysis (PLS-DA) were conducted to uncover significant variations between the different diet groups. PCA analyses were performed using the factoextra 1.0.7 package on the data from separate days, as well as on the whole dataset. The results of the PERMANOVA analysis, performed with the adonis2 function from vegan package, were utilized to quantify the most significant separation for each independent time point (day of fecal sample collection). The data for the supervised multivariate analysis were subset into two sets: days 4-47 and days 51-96, indicating the time before and after the diet switch. PLS-DA plots were built using the mixOmics 6.22.0 package, where diet groups were assigned as response variables. The evaluation of PLS-DA model performance was carried out using leave-one-out validation to determine the optimal number of components to be used. Discriminating metabolites were identified through variable importance in projection (VIP) scores > 1.

In silico chemical classification. From the initially identified 5731 features, only 606 compounds were successfully matched with public libraries for annotation. To enhance the identification of unknown compounds, annotation was additionally propagated by employing the *in silico* tools Canopus and SIRIUS[36,37]. The mgf result file from MZmine 3.4 as uploaded to the SIRIUS application, and specific parameters were selected, including the following: Database: none, Mass deviation of the fragment peaks in ppm: 5, Maximum number of candidates in the output: 10, Ion mode: positive, Analysis used: Orbitrap, Schema: Auto, Minimum number of MS/MS peaks: 1. As a result, an additional 5550 compounds were *in silico* annotated, propagating identification of previously unknown metabolites.

Data visualization. Molecular networking results obtained from GNPS were visualized in Cytoscape[39], with nodes represented as pie charts. The color distribution in each pie chart corresponded to the relative abundance of metabolites in each diet type. To visualize the dose dependence of selected metabolites on dietary iron, the santaR 1.2.3 package was employed to plot

feature abundance against time, and the gplots 3.1.3 package was used to generate heatmaps.

Whole Genome Sequencing. The UC San Diego Microbiome Core performed nucleic acid extractions utilizing previously published protocols[73]. Briefly, samples were purified using the MagMAX Microbiome Ultra Nucleic Acid Isolation Kit (Thermo Fisher Scientific, USA) and automated on KingFisher Flex robots (Thermo Fisher Scientific, USA). Blank controls and mock communities (Zymo Research Corporation, USA) were included and carried through all downstream processing steps. DNA was quantified using a PicoGreen fluorescence assay (Thermo Fisher Scientific, USA) and metagenomic libraries were prepared with KAPA HyperPlus kits (Roche Diagnostics, USA) following manufacturer's instructions and automated on EpMotion automated liquid handlers (Eppendorf, Germany). Sequencing was performed on the Illumina NovaSeq 6000 sequencing platform with paired-end 150 bp cycles at the Institute for Genomic Medicine (IGM), UC San Diego.

Microbiome Data Analysis. Demultiplexed fastq files provided by the UC San Diego Microbiome Core were uploaded to Qiita[74] (Study ID 15161). Files were processed using the default workflow, involving trimming of the autodetected adapters, filtering of reads mapping to the mouse genome, and the generation of the operational genomic unit (OGU) and KEGG orthologous (KO) tables and using Woltka[75]. R version 4.2.2 (R Foundation for Statistical Computing, Vienna, Austria) was used for the downstream analysis. Data was manipulated using `phyloseq v 1.42.0` and OGUs were collapsed at species level. Data was centered log ratio transformed using the decostand function from `vegan v 2.6-4` and taxa with zero variance between samples was removed using the nearZeroVar function from `caret v 6.0-94`. PCA was performed using `mixOmics v 6.22.0` and centroid separation was evaluated using PERMANOVA from the adonis2 function from `vegan v 2.6-4`. Group dispersion was checked for satisfying PERMANOVA assumptions using the function betadisper from `vegan v 2.6-4`. PLS-DA was performed using `mixOmics v 6.22.0` and models were evaluated using leave-one-out (loo) cross validation to calculate the classification error rate (CER). Finally, pairwise differential abundance analysis for taxa and enzymes was performed using ALDEx2[76] from `CoDaSeq v 0.99.6`. Taxa with p value < 0.05 were retained for interpretation.

Acknowledgments:

This research was supported by the Gordon and Betty Moore Foundation and University of Denver start-up funds (ATA, AK, & PCD). Work in MR lab was supported by NIH grant AI126277 (MR & HZ). This publication includes data generated at the UC San Diego IGM Genomics Center utilizing an Illumina NovaSeq 6000 that was purchased with funding from a National Institutes of Health SIG grant (#S10 OD026929). We also thank Professor Catherine Durso for statistical discussion, troubleshooting, and advice.

Data availability:

All untargeted LC-MS/MS data used in this study are publicly available at MassIVE (https://massive.ucsd.edu/) under the following accession numbers: MSV000084783 (doi:10.25345/C51M4J). The feature-based molecular networking job is publicly available at GNPS: https://gnps.ucsd.edu/ProteoSAFe/status.jsp?task=d35b583c2cf3435289a0aca8de4df4dd.